



**HAL**  
open science

# Riemannian Clustering of PolSAR Data using the Polar Decomposition

Madalina Ciuca, Gabriel Vasile, Marco Congedo, Michel Gay

► **To cite this version:**

Madalina Ciuca, Gabriel Vasile, Marco Congedo, Michel Gay. Riemannian Clustering of PolSAR Data using the Polar Decomposition. 2022. hal-03839678v1

**HAL Id: hal-03839678**





**<https://hal.science/hal-03839678v1>**

Preprint submitted on 4 Nov 2022 (v1), last revised 10 Nov 2023 (v3)

**HAL** is a multi-disciplinary open access archive for the deposit and dissemination of scientific research documents, whether they are published or not. The documents may come from teaching and research institutions in France or abroad, or from public or private research centers.

L'archive ouverte pluridisciplinaire **HAL**, est destinée au dépôt et à la diffusion de documents scientifiques de niveau recherche, publiés ou non, émanant des établissements d'enseignement et de recherche français ou étrangers, des laboratoires publics ou privés.

# Riemannian Clustering of PolSAR Data using the Polar Decomposition

Madalina Ciuca<sup>\*†</sup> , *Graduate Student Member, IEEE*, Gabriel Vasile<sup>\*</sup> , *Senior Member, IEEE*, Marco Congedo<sup>\*</sup> , Michel Gay<sup>\*</sup> , *Senior Member, IEEE*,

**Abstract**—In this manuscript we propose an algorithm for unsupervised classification of PolSAR data, on the manifold of Hermitian positive definite matrices obtained from the polar decomposition of the scattering matrix. The method uses a geodesic metric for evaluating similarity of Hermitian matrices and performs unsupervised classification for both coherent and incoherent targets. Monostatic, full-polarimetric, real and simulated datasets are used for testing the proposed method. With Gaussian clutter, the technique is able to retrieve classification maps similar to those obtained using the standard Wishart algorithm. A refinement of classification results is shown for a simulated dataset with 4 classes. While the Wishart classifier attains an average class accuracy of almost 97%, the proposed method reaches almost 99%. For real PolSAR data, the final classification better preserves the texture information of the original image. As a result, an improved separation is shown between nearby areas of lower intensity, as for example vegetation fields.

**Index Terms**—PolSAR, scattering matrix, polar decomposition, Hermitian factor, unitary polar factor, Riemannian distance, affine invariant metric, geodesics, Riemannian k-means, PolBaRi, Bretigny, X-Band.

## I. INTRODUCTION

THE interpretation of Polarimetric Synthetic Aperture Radar (PolSAR) data is mainly based on the extraction of parameters, to which physical/geometrical properties are assigned. Classical descriptors of PolSAR images are the scattering matrix and/or the covariance/coherency matrices.

The decomposition algorithms proposed for parameters extraction can be divided into two general categories: coherent and incoherent, depending on whether they use the scattering or the covariance<sup>1</sup> matrices, respectively. In PolSAR, the backscattering depends primarily on

Manuscript received Month Day, Year; revised Month Day, Year. M. Ciuca is with Laboratoire Grenoble Images Parole Signal Automatique (GIPSA-lab), Univ. Grenoble Alpes, CNRS, Grenoble INP, 38000 Grenoble, France, and with the Department of Telecommunications, University Politehnica of Bucharest, 060032 Bucharest, Romania. G. Vasile, M. Congedo and M. Gay are with Laboratoire Grenoble Images Parole Signal Automatique (GIPSA-lab), Univ. Grenoble Alpes, CNRS, Grenoble INP, 38000 Grenoble, France (email: surname.name@grenoble-inp.fr).

<sup>1</sup>also coherency. In the current text, mentioning one, automatically implies the other. Mathematical definitions are reported in Annex A.

the nature of the imaged targets and on the dimension of the resolution cell. The information from only the target scattering vectors is often insufficient for reliable polarimetric features extraction. With distributed targets, the backscattering is characterized by incoherent target decompositions, obtained by means of PolSAR covariance matrices. As a downside, the resolution of the original image can be greatly degraded and small features can no longer be recovered in incoherent processing due to complex multi-looking.

This paper proposes a new method that exploits directly the scattering matrix by applying the polar decomposition. The Hermitian factors, inherently located on a Riemannian manifold, are used for classification. This method can be applied with both coherent and incoherent targets. Experimental results show that it can recover the texture-driven information and details lost when exploiting second order statistics and improve, as a result, the interpretability of the original polarimetric dataset. We compare the classification results of the proposed method with those obtained using the classical Wishart method. For validation, both simulated and real full-polarimetric PolSAR data are employed.

The remainder of this paper is organized as follows. Section II offers some background on the use of the polar decomposition. It then focusses on defining concepts and tools necessary for applying the Riemannian manifolds theory with PolSAR data. Finally, it introduces the description of our proposed method. Section III analyses the experimental results. The conclusion and perspectives for future work are discussed in Section IV.

## II. FROM POLAR DECOMPOSITION TO CLASSIFICATION ON A RIEMANNIAN MANIFOLD

### A. The polar decomposition

Any complex square matrix  $\mathbf{S} \in \mathbb{C}^{n \times n}$  can be decomposed using the polar decomposition as the product of two factors: a *unitary matrix* ( $\mathbf{U}$ ,  $\mathbf{U}\mathbf{U}^H = \mathbf{I}$ ,  $\mathbf{U} \in \mathbb{C}^{n \times n}$ ) and a *Hermitian matrix* ( $\mathbf{H}$ ,  $\mathbf{H}^H = \mathbf{H}$ ,  $\mathbf{H} \in \mathbb{C}^{n \times n}$ ).  $\mathbf{H}$  is positive semi-definite (PSD), thus we have  $\mathbf{v}^H \mathbf{H} \mathbf{v} \geq 0$

75 for any nonzero column with complex elements vector<sup>1</sup>,  
 76  $\mathbf{v} \in \mathbb{C}$ .  $\mathbf{U}$  is the nearest unitary matrix to  $\mathbf{S}$  in any  
 77 unitarily invariant norm [1]. The influence of the two  
 78 factors is interpreted as follows: the unitary factor per-  
 79 forms a rotation, while the Hermitian factor acts as a  
 80 stretching/deformation.

81 There exist two different forms, with eq. 1 being known  
 82 as the left polar decomposition and eq. 2 as the right  
 83 polar decomposition:

$$84 \quad \mathbf{S} = \mathbf{U}\mathbf{H} \quad (1) \quad \mathbf{S} = \mathbf{K}\mathbf{U}. \quad (2)$$

85 With respect to the left/right Hermitian factors, we can  
 86 write:  $\mathbf{H} = \sqrt{\mathbf{S}^H\mathbf{S}}$  and  $\mathbf{K} = \sqrt{\mathbf{S}\mathbf{S}^H}$ .

87 From a mathematical perspective, the polar decompo-  
 88 sition has a close connection to the Singular Value  
 89 Decomposition (SVD), from which it can be computed.  
 90 As a direct consequence, this decomposition can be  
 91 inherently applied to any complex matrix. While the  
 92 Hermitian factor obtained from the decomposition is  
 93 always unique, the unitary term is unique only if matrix  
 94  $\mathbf{S}$  is non-singular.

95 In PolSAR, the polar decomposition has been gener-  
 96 ally used as a coherent technique, allowing feature  
 97 extraction from the scattering matrix,  $\mathbf{S} \in \mathbb{C}^{2 \times 2}$ . Since  
 98 there are no constraints in applying the factorization, it  
 99 can be used for both symmetric/asymmetric, or other-  
 100 wise, monostatic/bistatic scattering matrices.

101 The pioneering works of Carrea et al. [2], [3] have  
 102 initially described the behaviour of the two decomposi-  
 103 tion factors. The Hermitian positive semi-definite matrix  
 104 is referred as a "boost" matrix.

105 Reference [4], [5] express the scattering matrix polar  
 106 decomposition using the formalism of quaternions and  
 107 derive descriptive features from the polar factors. They  
 108 propose both a coherent approach on single-look (also, 1-  
 109 look) quad-pol(arimetric) data, as well as a generalization  
 110 for incoherent multi-look data.

111 In optical polarimetry, the polar decomposition splits  
 112 a complex  $2 \times 2$  Jones matrix in a retarder (i.e., the  
 113 unitary matrix) and a diattenuator (i.e., the Hermitian  
 114 matrix). The same significance is attributed to the two  
 115 products obtained from decomposing a nondepolarizing  
 116 Mueller matrix [6], while a generalized polar decom-  
 117 position (retarder, diattenuator and depolarizer factors  
 118 extraction) is further proposed for a general Mueller  
 119 matrix. Classification is performed coherently (i.e., in a  
 120 pixel-by-pixel manner) in [7], on real PolSAR data in  
 121 Mueller matrix format, following the above-mentioned  
 122 generalized polar decomposition model.

<sup>1</sup>Notation: Boldface is used for vectors and matrices, with the first  
 using lowercase and the second uppercase letters.

$\mathbf{I}$  denotes the identity matrix of size  $n \times n$ . Known operators are:  
 $(\cdot)^T$  as the transpose,  $(\cdot)^*$  as the complex conjugate and  $(\cdot)^H$  as the  
 conjugate-transpose.  $\|\cdot\|_F$  refers to the Frobenius norm, while  $|\cdot|$   
 is the absolute value.

123 In the proposed method, we use the polar decompo-  
 124 sition of the scattering matrix, but apply the clustering  
 125 technique only to the Hermitian terms. This effectively  
 126 remove the unitary factor, treated here as a nuisance  
 127 parameter. More details of the algorithm implementation  
 128 are offered in Subsection II-E.

## B. Riemannian manifold and corresponding distances

129 It is well known that positive-definite matrices are  
 130 naturally embedded in a non-linear, smooth differentiable  
 131 manifold. On such a manifold, the shortest path connect-  
 132 ing any two points is named a geodesic: it is not a straight  
 133 line, as in the Euclidean space, but a path which follows  
 134 the curvature of the space.

135 Applying a suitable metric on the tangent bundle  
 136 yields a Riemannian manifold,  $\mathbb{P}(n)$ . The best-known  
 137 metric used for the PSD manifold is the affine invariant  
 138 Riemannian metric (AIRM) [8].

139 For any two positive definite matrices  $\mathbf{A}$  and  $\mathbf{B}$ , AIRM  
 140 yields a closed-form distance measure

$$141 \quad d_{geod, \mathbb{P}(n)}(\mathbf{A}, \mathbf{B}) = \|\log(\mathbf{A}^{-1/2}\mathbf{B}\mathbf{A}^{-1/2})\|_F, \quad (3)$$

142 which can be interpreted as a similarity/dissimilarity cri-  
 143 terion. Operator  $\log(\mathbf{X})$  represents the matrix logarithm.  
 144 For positive-definite matrices it is usually computed  
 145 using the eigenvalue decomposition:  $\mathbf{X} = \mathbf{V}\mathbf{D}\mathbf{V}^H$ ,  $\mathbf{D} =$   
 146  $\text{diag}(\lambda_1, \lambda_2, \dots, \lambda_n)$  and the usual logarithm function.  
 147 Operator  $\text{diag}(\cdot)$  returns a diagonal matrix having the  
 148 elements inside parenthesis on the main diagonal. Then,  
 149  $\mathbf{D}_{log} = \text{diag}(\log(\lambda_1), \log(\lambda_2), \dots, \log(\lambda_n))$  and

$$150 \quad \log(\mathbf{X}) = \mathbf{V} \cdot \mathbf{D}_{log} \cdot \mathbf{V}^H. \quad (4)$$

151 The AIRM geodesic distance complies to several  
 152 invariance properties such as self-duality, congruence  
 153 invariance, joint homogeneity and determinant identity,  
 154 among others [8]. In particular, the congruence (or,  
 155 affine) invariance reads

$$156 \quad d_{geod, \mathbb{P}(n)}(\mathbf{J}\mathbf{A}\mathbf{J}^H, \mathbf{J}\mathbf{B}\mathbf{J}^H) = d_{geod, \mathbb{P}(n)}(\mathbf{A}, \mathbf{B}), \quad (5)$$

157 for any non-singular matrix  $\mathbf{J}$ .

158 For real PolSAR data, due the presence of noise (ther-  
 159 mal or speckle), the Hermitian factors of the observed  
 160 scattering matrices lie on the Riemannian manifold of  
 positive definite matrices with dimension  $n = 3$ . We can  
 associate to any general matrix  $\mathbf{H}$  in this space,

$$161 \quad \mathbf{H} = \begin{pmatrix} h_{11} & h_{12} \\ h_{12}^* & h_{22} \end{pmatrix}, \quad (6)$$

a point in  $\mathbb{R}^3$ , according to the mapping [9]:

$$162 \quad \mathcal{F}(\mathbf{H}) = \frac{1}{\sqrt{2}} [h_{12} + h_{12}^*, h_{22} - h_{11}, h_{22} + h_{11}]. \quad (7)$$

163 For  $m$  positive definite matrices  $\{\mathbf{H}_1, \mathbf{H}_2, \dots, \mathbf{H}_m\}$ ,  
 $m > 2$ , the Riemannian barycenter, i.e., geometric center

164 of mass or geometric mean, is a point  $\mathbf{H}_0$  which attains  
165 the minimum value of [10]

$$\arg \min_{\mathbf{H}_0} \sum_{i=1}^m d_{geod, \mathbb{P}(n)}(\mathbf{H}_0, \mathbf{H}_i)^2. \quad (8)$$

166 It is worth mentioning that the Riemannian mean  
167 presents some invariant properties, as follows [9]:

- 168 • *permutation invariance*:  
169  $\mathbf{H}_0$  is still the solution considering any rearrange-  
170 ment of the original set  $\{\mathbf{H}_i\}, i \in \overline{1, m}$ .
- 171 • *congruence invariance*:  
172 Changing the matrix set to  $\{\mathbf{V}\mathbf{H}_i\mathbf{V}^H\}, i \in \overline{1, m}$ ,  
173  $\mathbf{V}$  non-singular, the barycenter changes accordingly,  
174 becoming  $\mathbf{V}\mathbf{H}_0\mathbf{V}^H$ .
- 175 • *inversion invariance*:  
176  $\mathbf{H}_0^{-1}$  is the corresponding barycenter for the set of  
177 inverse matrices  $\{\mathbf{H}_i^{-1}\}, i \in \overline{1, m}$ .

178 It was shown that in the Riemannian manifolds of  
179 positive-definite matrices, the solution to the minimiza-  
180 tion problem in eq. 8 always exists and it is unique [11],  
181 [12]. While there is no closed-form solution, convergent  
182 results are obtained by iterative minimization methods  
183 [9], [12], as the gradient descent.

### 184 C. Unitary manifold and corresponding distances

185 On the manifold of unitary matrices,  $\mathbb{U}(n)$ , the  
186 geodesic distance between two generic matrices  $\mathbf{A}$  and  
187  $\mathbf{B}$  can be given as [11]:

$$d_U(\mathbf{A}, \mathbf{B}) = \|\log(\mathbf{A}^H \mathbf{B})\|_F. \quad (9)$$

188 The space of unitary matrices is a Lie group. Also, it is  
189 endorsed with a Lie algebra. Computing the barycenter of  
190  $p$  unitary matrices  $\{\mathbf{U}_1, \mathbf{U}_2, \dots, \mathbf{U}_p\}$  is addressed often  
191 in relation to the properties of this Lie space, but two  
192 main groups of methods are present in the literature.  
193 The first direction proposes to compute the barycenters  
194 by distance minimization (similar to eq. 8). The second  
195 direction, based on projections to the Lie algebra and  
196 back into the Lie group (retraction-lifting) [11] proposes  
197 a fixed point iteration algorithm. With both directions,  
198 no closed-form solutions are known.

199 The update rule for calculating the average of matrices  
200  $\{\mathbf{U}_j, j \in \overline{1, p}\}$  in the retraction-lifting manner is given  
201 by:

$$\mathbf{U}_{k+1} = \mathbf{U}_k \cdot \exp\left(\frac{1}{N} \sum_{j=1}^p \log(\mathbf{U}_k^H \mathbf{U}_j)\right). \quad (10)$$

202 Operator  $\exp(\cdot)$  represents the matrix exponential and  
203 is the inverse operation of  $\log(\cdot)$ .

204 Notice that, for computing the barycenter in the man-  
205 ifold of unitary matrices, a simple gradient descent may  
206 not always converge due to numerical problems. In

207 this work we focus on the Hermitian factors only and  
208 we compute the barycenter of unitary factors just for  
209 illustration purposes. Therefore, while more sophisticated  
210 algorithmic solutions exist, we did not implement them.

211 Given the interpretation of a unitary matrix as a  
212 rotation matrix, we argue there is a significant advantage  
213 in eliminating this rotation from the original scattering  
214 matrix.

### D. Hermitian matrices and Riemannian geometry in PolSAR

215 It has been more than a decade since the Riemannian  
216 manifold embedding is used with PolSAR data, exclu-  
217 sively in evaluating the coherency/covariance matrices.  
218 In the general literature, we have identified different  
219 methodologies proposed for this manifold embedding.  
220 Some methods operate directly on the Riemannian man-  
221 ifold ( $M_1$ , Table IV, Annex A-A), while others operate  
222 with projections (i.e., onto the tangent space or onto other  
223 known geometric spaces). The method proposed by the  
224 current paper fits the first direction. A short literature  
225 review, with techniques and applications from PolSAR  
226 exploiting directly the Riemannian embedding, is given  
227 below. In Table IV, Annex A-A, references that relate to  
228 the other types of methods are provided. 229

230 In [13], [14], Formont et al. challenge the use of the  
231 popular Wishart distance for measuring the similarity  
232 between PolSAR covariance matrices. They modify the  
233 Wishart unsupervised classification algorithm of [15] and  
234 introduce the AIRM metric for distance calculation and  
235 determining class membership of a certain pixel. 236

237 In [16], the AIRM distance is used in a binary partition  
238 tree algorithm for classifying covariance matrices of  
239 PolSAR/PolInSAR time-series, while [17] uses this same  
240 metric for determining the optimum cut of such partition  
241 trees. 241

242 For adaptive PolSAR speckle filtering, [18], [19] pro-  
243 pose a modified mean shift algorithm. The method uses  
244 a different geodesic distance measure, the log-Euclidean  
245 Riemannian metric and its corresponding gradient, when  
246 calculating the local maximum point required in the  
247 implementation. 247

248 Therefore  $M_1$ -type techniques are reported in PolSAR  
249 with both preprocessing (i.e., filtering) and classification  
250 applications performed in the space of  $n \times n, n \in \{3, 4\}$   
251 covariance matrices. 251

### E. Proposed and comparative methods

252 1) *PolBaRi+Riemannian k-means*: We propose a  
253 novel algorithm for unsupervised classification, which  
254 performs clustering on the Riemannian manifold of  
255 Hermitian polar factors. Three different processing  
256

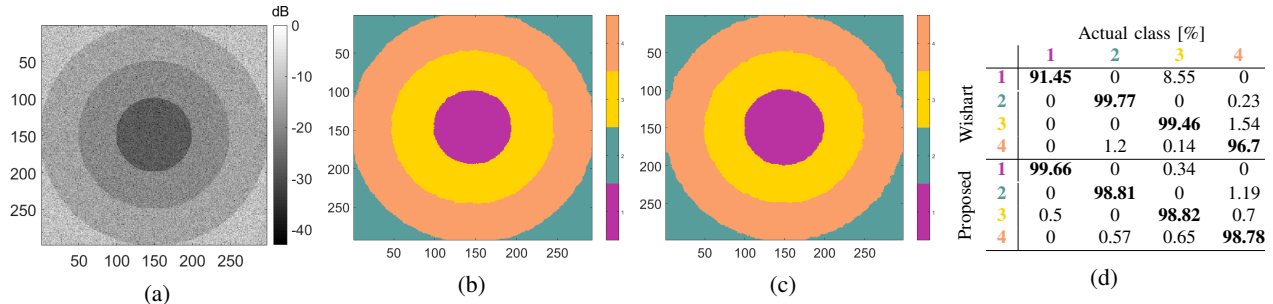


Fig. 1

Simulated data - Dataset 1.

(a) 1-look Span [dB]. (b) Wishart Classifier. (c) Proposed method: PolBaRi+Riemannian k-means. (d) Confusion matrix. (Colour correspondence:  $C_1$ : magenta, central circle;  $C_2$ : turquoise, corners;  $C_3$ : yellow, central annulus;  $C_4$ : light orange, exterior annulus).

257 stages can be identified:

258

259 — **Step 1:** The scattering matrix is decomposed using  
 260 the left<sup>1</sup> polar decomposition (eq. 1); the Hermitian and  
 261 unitary factors are obtained.

262 — **Step 2:** An identification of coherent scatterers  
 263 based on the 98<sup>th</sup> percentile criterion proposed by Lee  
 264 et al. [20] is performed, at first. As in the original  
 265 algorithm, a  $3 \times 3$  boxcar neighbourhood is used. The  
 266 pixels fulfilling the criterion are considered to represent  
 267 coherent targets. For them, no additional steps are  
 268 needed and the Hermitian factors are used directly for  
 269 clustering (Step 3). With all other pixels, barycenters  
 270 are otherwise computed. This is the analogous of a  
 271 N-look geometrical center of mass estimation in the  
 272 manifold of Hermitian polar factors. The barycenters are  
 273 computed through an iterative method (eq. 8) applied  
 274 in square, local, sliding neighbourhoods of fixed size.  
 275 The operation of evaluating the Riemannian barycenters  
 276 in the manifold of Hermitian factors is designated  
 277 henceforth by acronym *PolBaRi* (*POLar* decomposition  
 278 *BA*rycenters estimation on the *RI*emannian manifold).

279 — **Step 3:** The classical k-means algorithm is  
 280 an iterative, partitioning clustering technique which  
 281 separates the input data  $X = \{x_i\}, i \in [1, N]$  into  $K$   
 282 classes [21], [22]. The method operates by attributing  
 283 a sample  $x_i$  from the dataset to class  $K$  through the  
 284 minimization of a cost function  $\sum_{k=1}^K d(x_i, \mathbf{C}_k)$ . This  
 285 function calculates the sum of squared errors with  
 286 respect to each cluster centroid  $\mathbf{C}_k, k \in [1, K]$ .

287 A modified k-means algorithm is applied to our set  
 288 of points containing barycenters and coherent Hermitian  
 289 factors. The computation is kept into the native Riemannian  
 290 manifold of positive-definite matrices by choosing

<sup>1</sup>Since similar results have been obtained when considering alternatively the left or right polar decompositions, we refer hereafter exclusively to the use of the left polar factorization.

291 an appropriate distance measure. Therefore, the AIRM  
 292 metric is used to evaluate intercluster separation. Here,  
 293 the class centers are randomly initialised. Progressively,  
 294 each (barycenter) matrix from the set obtained in Step  
 295 2 is allocated to one of the  $K$  classes and the cluster  
 296 centers are updated. The operation is repeated until the  
 297 interclass transfer is lower than a predefined threshold.

298  
 299  
 300 The suggested algorithm is distinct from other PolSAR  
 301 Riemannian manifold methods. The state-of-art review in  
 302 Subsection II-D has evidenced the existence of PolSAR  
 303 studies using Riemannian distances and/or Riemannian  
 304 classifiers in the space of covariance/coherency matrices,  
 305 only. In contrast, we propose to obtain rotation invariant  
 306 Hermitian factors from the scattering matrix and manip-  
 307 ulate such matrices through geometrical averaging and  
 308 geometric-based clustering techniques.

309 2) **Wishart classifier:** The introduction of the Wishart  
 310 classifier has been a major milestone of PolSAR image  
 311 classification [15], [23]. To this day, the method remains  
 312 popular among unsupervised classification techniques  
 313 used in PolSAR. It operates on the set of covariance  
 314 matrices using as distance measure

$$d(\mathbf{A}, \mathbf{C}_k) = \ln |\mathbf{C}_k| + \text{tr}(\mathbf{C}_k^{-1} \mathbf{A}), \quad (11)$$

315 based on the property that the covariance matrices gener-  
 316 ally obey a complex Wishart distribution. Here,  $\mathbf{A}$  is a  
 317 generic covariance matrix and  $\mathbf{C}_k$  is the centroid of class  
 318  $K$ . The method has been shown to represent an optimal  
 319 Bayesian classifier considering that scattering vectors  
 320 are modelled by zero mean complex circular Gaussian  
 321 vectors, completely characterized by their covariance  
 322 matrix [23].

323 Usually, the algorithm operates with 8 distinct classes.  
 324 The centroids of these classes are not randomly ini-  
 325 tialized, but the  $H - \alpha$  decomposition is applied as a

prerequisite [24]. After performing the classification, the initial centroid values are obtained by averaging of all matrices attributed into the 8 zones of the  $H - \alpha$  plane.

### III. RESULTS AND DISCUSSION

The algorithm introduced in Subsection II-E is now evaluated on both simulated and real PolSAR data. Each case is addressed in a different subsection. The conventional Wishart classifier, applied on the space of covariance matrices, is used as a benchmark. In a different subsection we introduce a sample gradient computation technique based on the Sobel kernels, which evaluates the gradient directly on the manifold space.

#### A. Simulated datasets

Simulated polarimetric data is obtained through two different methods, as detailed by Subsections III-A1 and III-A2.

1) *Simulated data with different intensities and covariance matrices:* The first simulation technique is a classical method used in the literature [25]–[27]. It allows one to create synthetic responses of polarimetric channels with known statistics, i.e., having a known covariance/coherency matrix. In our example, we model four different Gaussian regions, arranged concentrically, as shown in Fig. 1a. The intensity is varied linearly from one region to another, with the region bounded by the image border and the second annulus having the highest intensity [26]. The simulated dataset serves as benchmark. The multivariate Gaussian clutter is still the most used statistical model for PolSAR data and represents the best-of-fit distribution for the case of homogeneous regions. With such a statistical model, the Wishart classifier is known to provide the optimum solution [23].

Figs. 1b and 1c display the results obtained using the Wishart classifier and the proposed method, respectively. For both algorithms, the number of expected classes has been provided as input. Table 1d contains the confusion matrices for each classification. The results are similar. With the proposed method, the identification of pixels inside a given class has at least a 98% accuracy, the true-positive percentages being here slightly more homogeneous than with the Wishart classifier.

2) *Simulated monostatic backscattering response of a dihedral:* With the second simulated dataset, the polarimetric signature of a monostatic right-angle dihedral is modelled. Using an electromagnetic simulation software (CST Microwave Studio), the scattered electric field of the dihedral can be obtained from a diverse range of monostatic directions. In the simulations, the object is placed in the centre of the coordinate system and

rendered from perfect electric conductor (PEC) material. A spherical coordinate system, described by parameters  $(\theta, \varphi)$  is used. The simulator returns the estimated complex, electric field response and subsequently, the elements from the scattering matrix (linear polarisation) are themselves estimated.

Fig. 2a displays the absolute value of the backscattered electric field, for the right-angle dihedral. The maximum value is obtained for the central point, with coordinates  $(\theta, \varphi) = (0^\circ, 0^\circ)$ . This corresponds to the monostatic canonical dihedral scattering direction, in a plane orthogonal to the dihedral's bisector.

In PolSAR, the response of a dihedral describes an elementary scattering mechanism known as double bounce. Identifying the mechanism in the multichannel SAR image is often done indirectly, by computing descriptive parameters. With coherent targets, one such parameter is the  $\alpha_{Cloud e}$  value [28]:

$$\alpha_{Cloud e} = \cos \left( \frac{1}{\sqrt{2}} \frac{|S_{hh} + S_{vv}|}{\sqrt{SPAN(\mathbf{S})}} \right)^{-1}, \quad (12)$$

which is fixed at  $90^\circ$  for the double bounce case. In Fig. 2b the  $\alpha_{Cloud e}$  parameter is estimated at each incidence/scattering direction. It is observed that the deviation from the theoretical value remains acceptable ( $\alpha_{Cloud e} \in [85^\circ, 90^\circ]$ ) for monostatic directions  $\theta, \varphi \in [-45^\circ, 45^\circ]$ . In contrast, for very skewed directions (incidence/scattering predominantly on the exterior edges of the two plates composing the dihedral), the mechanism changes, as expected.

In order to account for noise variation, we do not use directly this simulated data for PolBaRi+Riemannian k-means classification. Instead, at each pixel, multiple Gaussian estimates of the monostatic polarimetric channels are generated by the same method used for Simulated Dataset 1. After this stage, the PolBaRi estimation is performed at each pixel and then, the Riemannian k-means is applied. The number of classes is varied between 2-5 (Figs. 2c-f) in order to test the results. It is interesting to observe that the classification is persistent in identifying the two principal classes corresponding to the extreme scattering mechanisms of Fig. 2b. We refer here to the central region of uniform scattering mechanism (in yellow), which corresponds to the double bounce response, as confirmed by the  $\alpha_{Cloud e}$  parameter (Fig. 2b), and the second mechanism (i.e., single bounce), identified at the four exterior corners.

We extract a data profile cut along the middle horizontal line in Fig. 2b (position marked on left-side with green arrow). This corresponds to backscattering directions presenting right/left variations in azimuth angle, with respect to the monostatic canonical position for the dihedral.

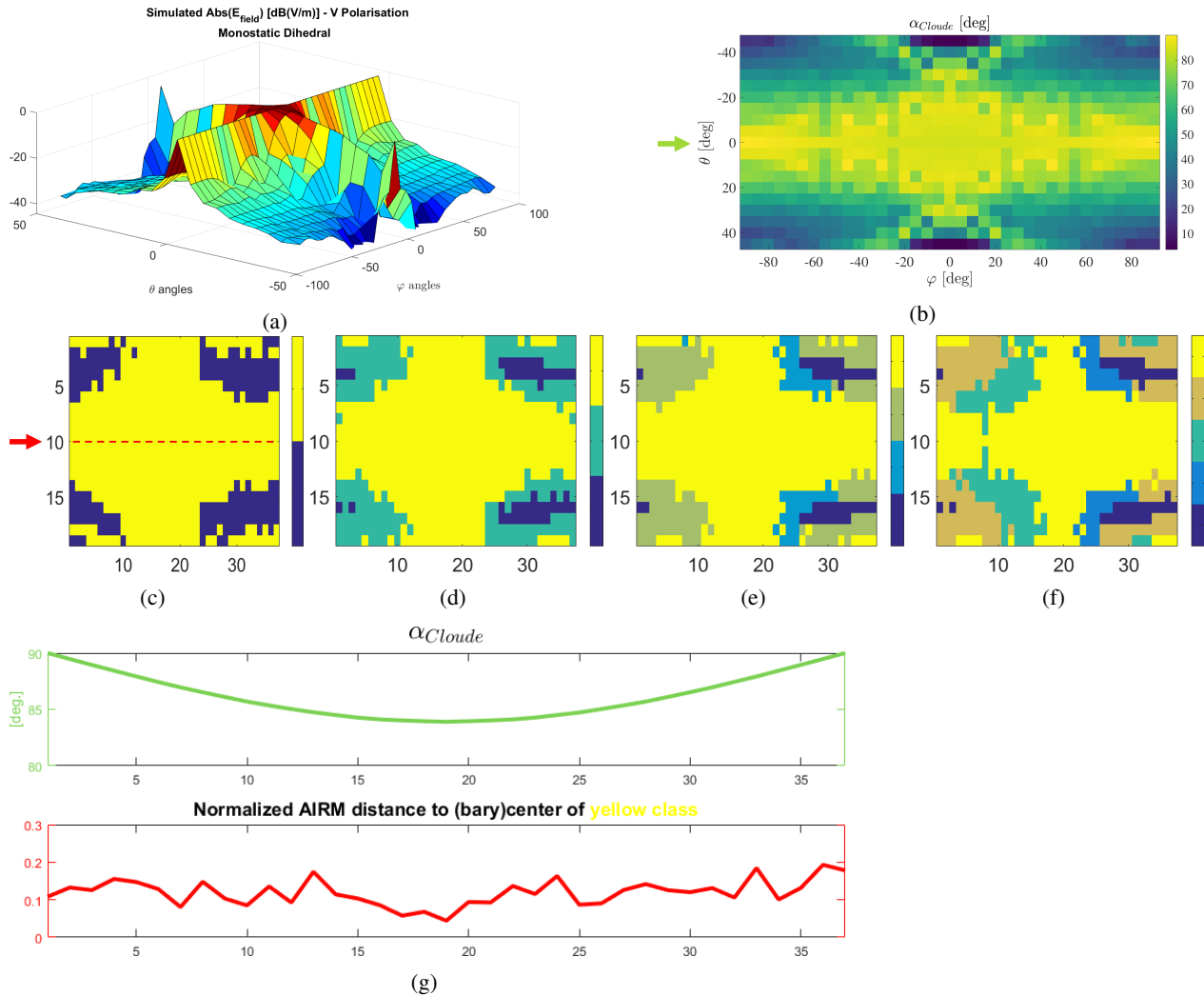


Fig. 2

Simulated data - Dataset 2.

(a) Absolute value of the scattered  $E_{field}$ , estimated by the simulation software. (b)  $\alpha_{Cloud}$  angles from estimated scattering matrices. (c-f) Riemannian k-means clustering result (variable number of classes between 2-5).

(g) *Upper*:  $\alpha_{Cloud}$  profile cut variation; *Lower*: Riemannian distance between barycenters along red profile cut (c) and yellow class centroid.

428 The  $\alpha_{Cloud}$  values are displayed in the upper sub-  
 429 figure of Fig. 2g, in the same green colour. Considering  
 430 the Hermitian barycenter matrices along the same line  
 431 for the k-mean estimation with two classes (marked  
 432 with left-side red arrow and dashed line in Fig. 2c),  
 433 the Riemannian dissimilarity measure is computed and  
 434 displayed. The lower subfigure of Fig. 2g contains the  
 435 normalized AIRM distances between each of the selected  
 436 barycenters and the final Hermitian k-means centroid  
 437 of corresponding class (i.e., yellow class from Fig. 2c).  
 438 While the manifold normalized distance (red, Fig. 2g)  
 439 presents a random variation, that of the  $\alpha_{Cloud}$  green  
 440 curve is quite deterministic. This is plausibly influenced

441 by the two distinct methods based on which the data was  
 442 obtained. The  $\alpha_{Cloud}$  parameter is evaluated directly  
 443 on the scattering matrices estimated from the electro-  
 444 magnetic simulator, while the PolBaRi method applied  
 445 to multiple Gaussian samples is used for computing the  
 446 barycenters.

447 It can be inferred that both parameters offer an iden-  
 448 tification with high confidence level of the scattering  
 449 mechanism and clustering group, respectively. However,  
 450 the dissimilarity measure has a much lower standard  
 451 deviation than that of the coherent alpha parameter.

### B. Manifold Gradient with Sobel Kernel

For an extended evaluation of Hermitian and unitary barycenters, a gradient assessment is performed in each manifold space. Because the convergence did not occur in all cases for the algorithm employed in evaluating the unitary barycenters, a coherence mask selection is used, so that the points which do not satisfy convergence are masked out. As example, for Dataset 2 such points are marked with red in Fig. 3c. They represent around 21.5% of all evaluated points, with the rest verifying unitary convergence.

TABLE I  
Vertical Sobel kernel.

-1	0	1
-2	0	2
-1	0	1

TABLE II  
Horizontal Sobel kernel.

-1	-2	-1
0	0	0
1	2	1

The classical Sobel operator [29], [30], known primarily for edge detection in digital image processing, proposes a sample computation of the first order derivative. It operates with two  $3 \times 3$  kernel filters (Tables I, II). Each of them, used as a sliding window, is convoluted with a spatial neighbourhood of the same size to produce the vertical and horizontal gradient components.

We propose an adaptation for gradient computation on the (Hermitian/unitary) manifold. The same weights as in the Sobel kernels multiply barycenter matrices within a  $3 \times 3$  spatial neighbourhood, while an adequate metric is used for distance dissimilarity (AIRM with Hermitian matrices and eq. 9 with unitary matrices). Both the vertical ( $\mathbf{G}_V$ ) and the horizontal ( $\mathbf{G}_H$ ) manifold gradient components are evaluated.

Considering  $\mathbf{P}^{i,j}$  a (Hermitian/unitary) barycenter matrix located on row  $i$ , column  $j$ . The following expressions can be written:

$$\mathbf{G}_H^{i,j} = d(\mathbf{P}_{\uparrow}^{i,j}, \mathbf{P}_{\downarrow}^{i,j}), \quad \mathbf{G}_V^{i,j} = d(\mathbf{P}_{\rightarrow}^{i,j}, \mathbf{P}_{\leftarrow}^{i,j}), \quad (13) \quad (14)$$

where

$$\mathbf{P}_{\uparrow}^{i,j} = \mathbf{P}^{i-1,j-1} + 2\mathbf{P}^{i-1,j} + \mathbf{P}^{i-1,j+1} \quad (15)$$

$$\mathbf{P}_{\downarrow}^{i,j} = \mathbf{P}^{i+1,j-1} + 2\mathbf{P}^{i+1,j} + \mathbf{P}^{i+1,j+1} \quad (16)$$

$$\mathbf{P}_{\leftarrow}^{i,j} = \mathbf{P}^{i-1,j-1} + 2\mathbf{P}^{i,j-1} + \mathbf{P}^{i+1,j-1} \quad (17)$$

$$\mathbf{P}_{\rightarrow}^{i,j} = \mathbf{P}^{i-1,j+1} + 2\mathbf{P}^{i,j+1} + \mathbf{P}^{i+1,j+1}. \quad (18)$$

and the magnitude of the gradient is

$$\mathbf{G} = \sqrt{\mathbf{G}_H^2 + \mathbf{G}_V^2}. \quad (19)$$

For simulated Dataset 2, Figs. 3a and 3b display the absolute values of the manifold Sobel gradient (eq. 19) for the Hermitian and unitary barycenters, respectively. While the Hermitian gradient reproduces the structural

information of the simulated data, there is no visual information offered by the unitary gradient. Such result offers a strong motivation for the choice of using only the Hermitian factor information for data clustering.

### C. Real dataset

Here we illustrate the performance of the proposed algorithm on real monostatic PolSAR data. The dataset is full-polarimetric, obtained by the Onera RAMSES airborne X-Band radar instrument, over a test site in Brétigny-sur-Orge (France). It is characterized by a resolution of approximate 1.5 m, in both azimuth and range [31].

Foremost, the discussion is extended for the Hermitian and unitary barycenters assessment, now in the context of the real dataset. Afterwards, the results for the clustering method are evaluated.

1) *Gradient of Hermitian barycenters and unitary barycenters parameter estimation:* Fig. 4 presents the Hermitian barycenters Sobel gradient estimate (absolute value, [dB]) for the Brétigny dataset. The shape of the three important structures from the image (horizontal West-Center, left-oblique North-West and right-oblique North-East) is easily distinguished, as well as field contours. Moreover, bright pixels are clearly isolated. A threshold selection may allow for an extraction of coherent scatterers positions similar to that obtained by the 98<sup>th</sup> percentile criterion.

While the gradient evaluation shows again that the unitary barycenters do not provide contextual information (data not shown), we aim to assess if they offer any other relevant information. The points for which unitary barycenters are not convergent are masked-out and can be observed in white in Figs. 5a and 5b.

Starting from a complex unitary matrix,  $\mathbf{U} \in \mathbb{C}^{2 \times 2}$ , with

$$\mathbf{U} = \begin{pmatrix} u_{11} & u_{12} \\ u_{21} & u_{22} \end{pmatrix} = \begin{pmatrix} |u_{11}| \cdot e^{i\varphi_1} & |u_{12}| \cdot e^{i\varphi_2} \\ |u_{21}| \cdot e^{i\varphi_3} & |u_{22}| \cdot e^{i\varphi_4} \end{pmatrix}. \quad (20)$$

The phase normalized unitary matrix  $\mathbf{U}_{ph-}$  can be written in parametric form [32]:

$$\mathbf{U}_{ph-} = \mathbf{U} \begin{pmatrix} e^{-i\varphi_1} & 0 \\ 0 & e^{-i\varphi_4} \end{pmatrix} = \begin{pmatrix} |u_{11}| & |u_{12}| \cdot e^{i(\varphi_2 - \varphi_4)} \\ |u_{21}| \cdot e^{i(\varphi_3 - \varphi_1)} & |u_{22}| \end{pmatrix} \quad (21)$$

$$= \begin{pmatrix} \cos\theta & -\sin\theta \cdot e^{-i\phi} \\ \sin\theta \cdot e^{i\phi} & \cos\theta \end{pmatrix} \quad (22)$$



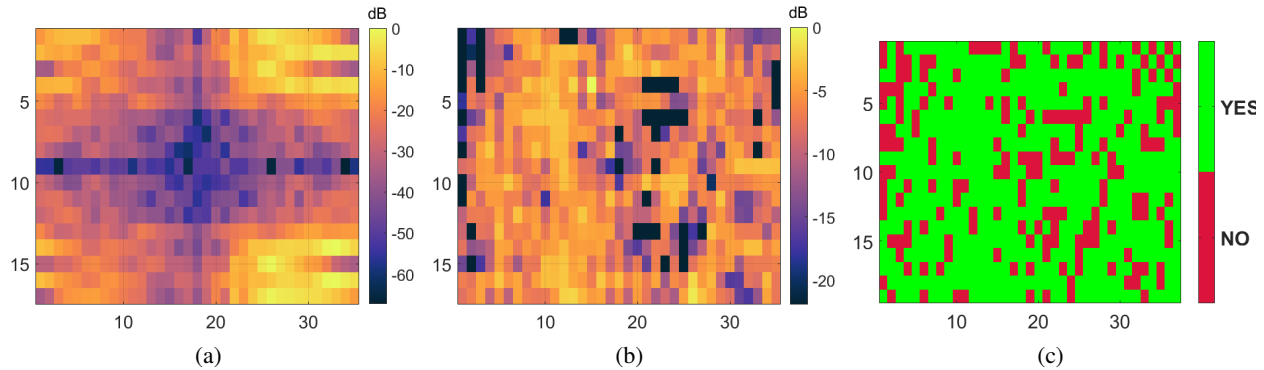


Fig. 3  
 Simulated data - Dataset 2. (a) Hermitian barycenters gradient - magnitude [dB]. (b) Unitary gradient - magnitude [dB]. (c) Convergence mask for unitary barycenters.

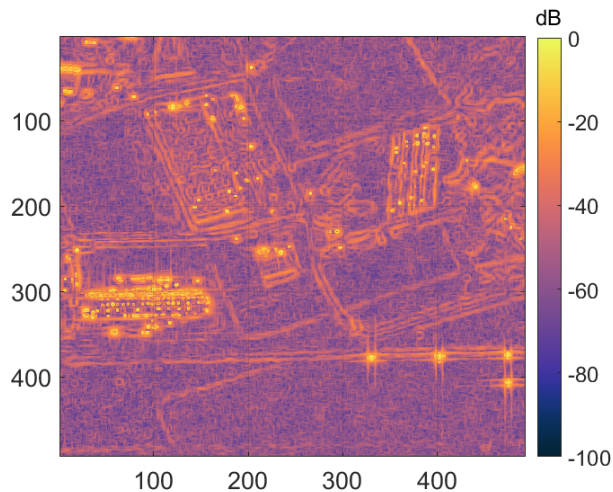


Fig. 4  
 Brétigny Dataset. Riemannian gradient using the Sobel filter kernels - Magnitude [dB].

525 After performing the phase normalization, as per eq.  
 526 21, the angular  $\theta$  and phase  $\phi$  parameters are easily  
 527 obtained for the unitary barycenters of the real dataset.  
 528 The results are in Fig. 5a and Fig. 5b, respectively,  
 529 with histograms below the main figures. It is to be mentioned  
 530 that with the Brétigny dataset about 25% of the image  
 531 pixels do not attain unitary barycenter convergence.

532 The  $\theta$  angle parameter takes values below  $25^\circ$  (Fig.  
 533 5c), while the phase is normally spread in the entire  $[0,$   
 534  $180^\circ]$  interval (Fig. 5d). As example, we can observe  
 535 the zone corresponding to the building located West-  
 536 Center, where multiple coherent scatterers are present  
 537 (red ellipse selection). There, the  $\theta$  values approach  
 538 zero degrees. The phase values present also an extreme  
 539 (i.e.  $\pm 180^\circ$ ). Such observations indicate that the phase  
 540 normalized unitary barycenters at those locations are  
 541 (almost) identity matrices. In turn, this may also im-

ply that the original unitary polar factors, used in the  
 barycenters calculation, are themselves close to identity.  
 For such a case, the Hermitian polar factors are  
 completely descriptive and (almost) equal to the original  
 scattering matrices. Moreover, this confirms the choice  
 from the design of the PolBaRi algorithm of performing  
 the pre-selection of coherent scatterer and attributing to  
 those locations directly the Hermitian factor, without  
 barycenter estimation.

Removing the effect of rotations imposed on the line-  
 of-sight backscattering direction as well as the search  
 of rotation invariant descriptors is of particular interest  
 in polarimetric radar applications. The topic has a  
 significant line of work associated for both coherent and  
 incoherent PolSAR decompositions [33], [34]. We have  
 shown that the unitary matrices can be described by two  
 random phases and two parametric values (an angle and  
 a phase). With coherent scatterers, discarding the unitary  
 polar factor does not produce significant changes, while  
 for other scatterers the removal of unwanted rotations  
 from the original scattering matrix is highly beneficial.  
 Evidence from both simulated and real data shows that  
 the contextual and spatial information is preserved by  
 the Hermitian polar term. Such observations legitimize  
 the key role of the Hermitian barycenters with the  
 proposed classification method.

Figs. 6a and 6b compare the results of two different  
 boxcar "averaging" operations. Each image displays the  
 absolute values inside each first channel from the data  
 cube results.

For obtaining Fig. 6a, the arithmetic mean of scattering  
 matrices (Brétigny dataset) has been computed inside  
 a  $7 \times 7$ , locally moving window. Otherwise, Fig. 6b  
 contains absolute values (log scale) of the first element  
 of the estimated Hermitian barycenters.

In the first picture (first row, left image, Fig. 6), there

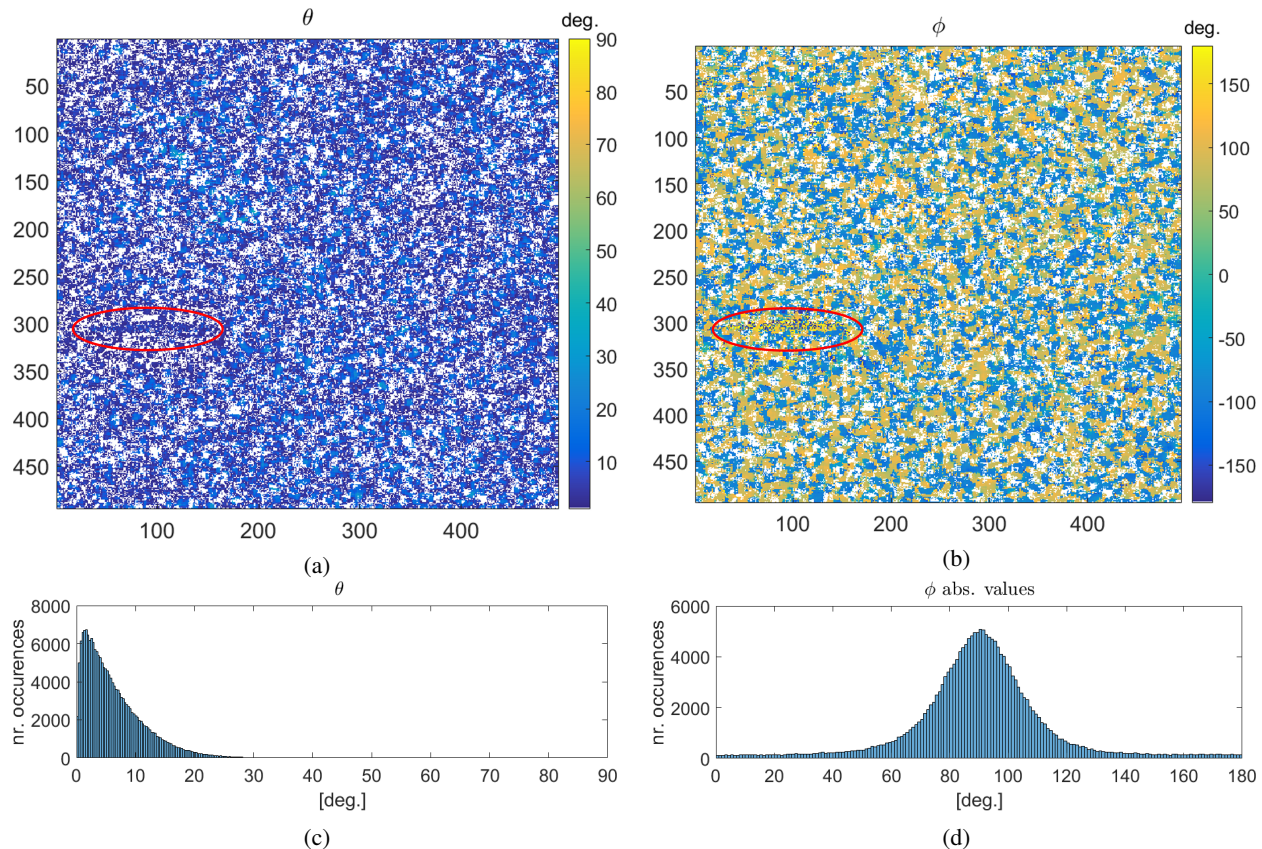


Fig. 5

Brétigny Dataset. (a) Angles obtained from the normalized unitary barycenter matrices [degrees]. (b) Phase values obtained from the normalized unitary barycenter matrices [degrees]. (c) Histogram of angles from (a) (excluding white-masked values). (d) Histogram of absolute phases from (b) (excluding white-masked values).

579 is a low dynamic range, with amplitude levels of the  
 580 different zones being mixed up. Only scattering points,  
 581 originally of high amplitude, remain clearly visible. On  
 582 the contrary, a higher dynamic range is evident in the  
 583 neighbouring barycenter image (first row, right image,  
 584 Fig. 6). Alongside the scatterers of high intensity, the  
 585 shape and structure of other parts from the original image  
 586 are clearly distinguishable, for example with vegetation  
 587 parcels and roads.

588 The visual inspection proposed between a spatial  
 589 arithmetic average of scattering matrices and a spatial  
 590 geometric estimation of a Hermitian centroids shows  
 591 superior results for the second approach. In light of this  
 592 comparison, a similarity may be drawn to the results from  
 593 [35]. The reference compares the difference between  
 594 arithmetic and geometric averages of single channel  
 595 multi-temporal SAR series. Improved results in terms of  
 596 speckle variation and signal to noise ratio are reported  
 597 for the geometric mean computation, as long as the SAR  
 598 images from the acquisitions stack remain similar, with  
 599 no significant permanent changes.

## 2) Classification results:

600  
 601 In the following, we compare the clustering results  
 602 obtained by the proposed and benchmark algorithms on  
 603 the real X-Band dataset. Both implementations require a  
 604 spatially moving window averaging operation. With the  
 605 Wishart implementation this is performed in a boxcar  
 606 neighbourhood of coherency matrices, while PolBaRi  
 607 requires it for the Hermitian barycenters estimation. The  
 608 same size of the moving window,  $7 \times 7$ , is used with  
 609 both implementations.  
 610

611 Figs. 6c and 6d display the classification results  
 612 for the classical Wishart and the proposed method,  
 613 respectively. The Wishart estimation operates with 8  
 614 classes. The same number has been considered for the  
 615 PolBaRi+Riemannian k-means implementation. The  
 616 classes are sorted in an ascending order (blue to yellow).  
 617

618 The global positioning of classes in the two images is  
 619 similar. One major visual difference concerns the bow-  
 620 shaped field in the North of Fig. 6d, which is assigned to

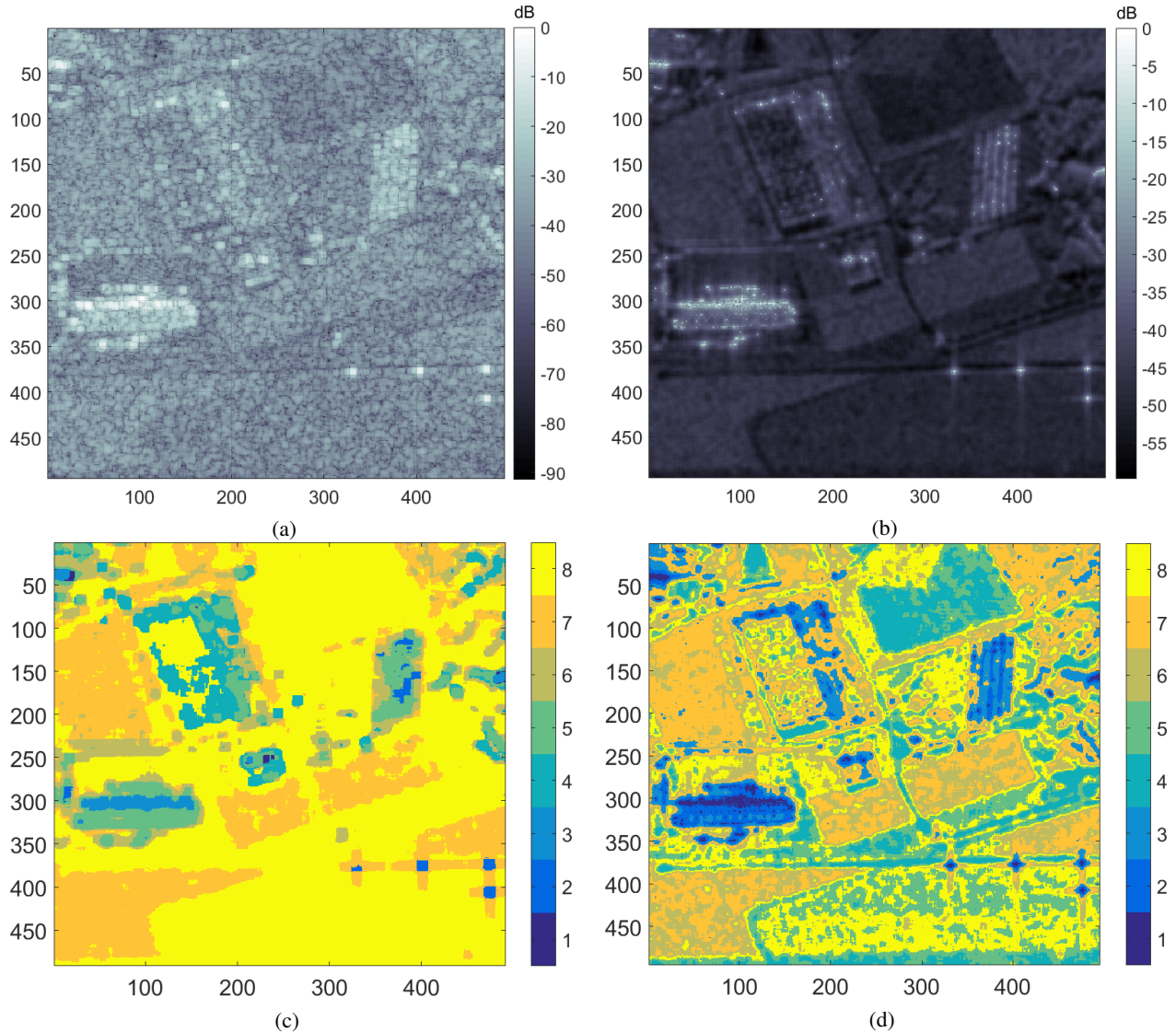


Fig. 6  
 Brétigny Dataset. (a)  $S_{11}$  boxcar average (amplitude, [dB]). (b)  $h_{11}$  barycenters (amplitude, [dB]). (c) Wishart classifier result. (d) PolBaRi+Riemannian k-means classification result.

621 a distinct class. This is the case with other small zones,  
 622 attributed by the Wishart classification to the 8<sup>th</sup>, yellow  
 623 class. Overall, the classification of coherent scatterers  
 624 appears to be enhanced by the PolBaRi+Riemannian k-  
 625 means method.

626 Considering as examples the horizontal West-Center  
 627 oriented building and the oblique North-East parking  
 628 space, the proposed method identifies, at the locations,  
 629 classes in close proximity while the Wishart classifier  
 630 brings more distant ones together. However, as the final  
 631 scattering mechanism interpretation may not be quite  
 632 the same for the two classifiers and in the absence of  
 633 a ground truth for the dataset acquisition, the truthful  
 634 validation of classes proximity is not possible.

635 Without doubt, the most striking difference in the  
 636 interpretation offered by the two classifiers, is textural.  
 637 The Wishart result is unduly smooth, largely homoge-  
 638 neous, while the proposed algorithm provides a more  
 639 heterogeneous result, conserving some of the texture and  
 640 details of the original image. For example, in the left-  
 641 side of the parking space (North-East), near the road  
 642 border, there is an area covered by trees. The Wishart  
 643 classifier identifies a small group of trees to the south  
 644 of the parking lot and where some pixels of higher  
 645 intensity are present, while identification is minimum  
 646 in the area left to the parking lot. Contrastingly, the  
 647 proposed method better represents the information from  
 648 the area, even if the pixels are of lower intensity. As

649 second example, one can observe that the roads (contours  
 650 in Fig. 4) blend with the background yellow class in the  
 651 Wishart classification, whereas they are clearly distin-  
 652 guishable in the PolBaRi+Riemannian k-means result. In  
 653 the original image they too are represented by pixels of  
 654 lower intensity.

#### 655 IV. GENERAL REMARKS AND CONCLUSIONS

656 The proposed method, PolBaRi+Riemannian k-means,  
 657 is unique in several respects. It incorporates a coherent  
 658 technique operating on the original scattering matrix (i.e.,  
 659 the polar decomposition) and preserving the matrix form-  
 660 at (contrary to the incoherent decomposition methods  
 661 where data is firstly vectorized). It is to be emphasized  
 662 that the polar decomposition can be applied to both  
 663 symmetric and asymmetric scattering matrices and the  
 664 Hermitian factor is always unique. The method resembles  
 665 also the incoherent techniques, as it proposes a spatial  
 666 averaging processing on the (Riemannian) manifold for  
 667 calculating centroids of Hermitian factors. This allows  
 668 the applicability of the method even with distributed  
 669 targets inside a scene. The dissimilarity between two ma-  
 670 trices from the manifold is evaluated using a Riemannian  
 671 metric both for Hermitian polar factor centroids and in  
 672 the modified k-means algorithm.

673 In a distinct contribution of the paper, the Riemannian  
 674 metric is applied in the development of a sample gradient  
 675 algorithm based on the Sobel kernels. It is used for spatial  
 676 change evaluation with Hermitian and unitary barycenter  
 677 results. This implementation may prove useful for other  
 678 applications requiring a gradient computation on data  
 679 embedded in a Riemannian manifold structure.

680 The clustering algorithm's performance has been com-  
 681 pared against the well-known Wishart algorithm with  
 682 both simulated and real monostatic full-polarimetric im-  
 683 ages. The performance was shown to be competitive,  
 684 with simulated Gaussian clutter data - a case for which  
 685 the Wishart classifier is known to offer optimum re-  
 686 sults. With real data, it was illustrated that the Pol-  
 687 BaRi+Riemannian k-means result integrate more of the  
 688 intensity, texture and details of the original PolSAR im-  
 689 age. This allows for a better discrimination of structures  
 690 such as roads and vegetation.

691 Supplementary experiments are anticipated for better  
 692 understanding the geometric properties of the two factors  
 693 from the polar decomposition of PolSAR data, as well  
 694 as improvements in runtime of algorithms and with the  
 695 unitary factor convergence. As the method can be applied  
 696 with both symmetric and asymmetric scattering matrices,  
 697 an envisioned extension is for testing the results with data  
 698 from quasi-monostatic and bistatic systems.

#### APPENDIX A

699 For compact display and completeness, we present in  
 700 the current Appendix general formulas and information  
 701 not included in the paper's main body.  
 702

703 The radar scattering matrix in linear H, V polarisation  
 704 is written, as:

$$\mathbf{S} = \begin{bmatrix} S_{hh} & S_{hv} \\ S_{vh} & S_{vv} \end{bmatrix} \quad (23)$$

705 The polarimetric span (i.e., total power) of a pixel  
 706 refers to the squared Frobenius norm of the correspond-  
 707 ing scattering matrix:  $SPAN = |S_{hh}|^2 + |S_{hv}|^2 +$   
 708  $|S_{vh}|^2 + |S_{vv}|^2$ .

709 Table III reports the formulas of the sample covariance  
 710 (**C**) and coherency (**T**) matrices, which although heavily  
 711 mentioned in the paper, have not been formally intro-  
 712 duced. Angle brackets  $\langle \cdot \rangle$  denote ensemble averaging  
 713 in an imaging window.  $\mathbf{k}$  and  $\mathbf{k}_P$  are the monostatic  
 714 scattering vectors of so-called lexicographic and Pauli  
 715 bases.

#### 716 A. Evaluation methods and dissimilarity measures with 717 the Riemannian manifold

718 The geometric structure of an algebraic object may  
 719 sometimes impose optimal data manipulation methods,  
 720 as well as an appropriate distance measure.  
 721

722 Currently, for the Riemannian manifold, we can iden-  
 723 tify two major directions in the literature. On one hand,  
 724 there are methods which operate directly on the manifold  
 725 ( $M_1$  in Table IV). In such case, the shortest path between  
 726 two points (i.e., vectors/matrices) is always obtained  
 727 through a geodesic. On the other hand, there are methods  
 728 which avoid direct operations on the original Riemannian  
 729 manifold. According to [39], they are currently divided  
 730 into three categories: a) ( $M_{2a}$ ) which use the logarithmic  
 731 projection to the tangent space, b) ( $M_{2b}$ ) which propose  
 732 a higher dimensional embedding into a Reproducing  
 733 Kernel Hilbert Space (RKHS), and c) ( $M_{2c}$ ) which  
 734 perform a manifold-to-manifold mapping, given that the  
 735 second manifold space (not necessarily Riemannian) is  
 736 of lower dimension. The measures used by these methods  
 737 are distinct and depending on the mapping they can be  
 738 Euclidean, non-Euclidean or of geodesic type. Table IV  
 739 contains examples from the PolSAR literature in which  
 740 these manipulation methods have been applied, as well  
 741 as the chosen distance measures.

#### ACKNOWLEDGMENT

742  
 743 The authors would like to thank Fabien Ndagijimana  
 744 from the Grenoble Institute of Technology, Grenoble,  
 745 France, for providing access to the CST Microwave  
 746 Studio software.

TABLE III  
Sample covariance and coherency matrices formulas.

		Scattering vector (monostatic) $[k_1, k_2, k_3]^T$	Matrix form
Covariance	$\mathbf{C} = \frac{1}{N} \sum_{i=1}^N k_i k_i^{*T}$	$\mathbf{k} = [S_{hh}, \sqrt{2}S_{hv}, S_{vv}]^T$	$\begin{bmatrix} \langle  k_1 ^2 \rangle & \langle k_1 k_2^* \rangle & \langle k_1 k_3^* \rangle \\ \langle k_2 k_1^* \rangle & \langle  k_2 ^2 \rangle & \langle k_2 k_3^* \rangle \\ \langle k_3 k_1^* \rangle & \langle k_3 k_2^* \rangle & \langle  k_3 ^2 \rangle \end{bmatrix}$
Coherency	$\mathbf{T} = \frac{1}{N} \sum_{i=1}^N k_{P_i} k_{P_i}^{*T}$	$\mathbf{kP} = [S_{hh} + S_{vv}, S_{hh} - S_{vv}, \sqrt{2}S_{hv}]^T$	

TABLE IV  
Methods exploiting the geometry of the Riemannian manifold in PolSAR.

Methods type	In which space do they operate?	References in PolSAR	Metric/Measure
$M_1$	Directly on the manifold	[14], [16]	AIRM
$M_{2a}$	Projection to the Tangent Space	[18], [19]	Log-Euclidean
$M_{2b}$	Higher dimension embedding (Kernel Hilbert Spaces)	[36]–[38]	Stein divergence, Bartlett
$M_{2c}$	Lower dimension embedding	-	-

747

## REFERENCES

748

749

750

751

752

753

754

755

756

757

758

759

760

761

762

763

764

765

766

767

768

769

770

771

772

773

774

775

776

777

778

779

780

781

782

783

784

785

786

787

788

789

790

791

792

[11] S. Fiori and T. Tanaka, "An algorithm to compute averages on matrix lie groups," *IEEE Transactions on Signal Processing*, vol. 57, no. 12, pp. 4734–4743, 2009. 793

794

[12] A. Barachant, S. Bonnet, M. Congedo, and C. Jutten, "Multiclass brain–computer interface classification by riemannian geometry," *IEEE Transactions on Biomedical Engineering*, vol. 59, no. 4, pp. 920–928, 2012. 796

797

[13] P. Formont, J. Ovarlez, F. Pascal, G. Vasile, and L. Ferro-Famil, "On the extension of the product model in POLSAR processing for unsupervised classification using information geometry of covariance matrices," in *2011 IEEE International Geoscience and Remote Sensing Symposium*, 2011, pp. 1361–1364. 800

801

[14] P. Formont, J.-P. Ovarlez, and P. Frédéric, *On the Use of Matrix Information Geometry for Polarimetric SAR Image Classification*, F. Nielsen and R. Bhatia, Eds. Berlin, Heidelberg: Springer Berlin Heidelberg, 2013. [Online]. Available: https://doi.org/10.1007/978-3-642-30232-9\_10 805

806

[15] J.-S. Lee, M. Grunes, T. Ainsworth, L.-J. Du, D. Schuler, and S. Cloude, "Unsupervised classification using polarimetric decomposition and the complex Wishart classifier," *IEEE Transactions on Geoscience and Remote Sensing*, vol. 37, no. 5, pp. 2249–2258, 1999. 810

811

[16] A. Alonso-González, C. López-Martínez, and P. Salembier, "Pol-sar time series processing with binary partition trees," *IEEE Transactions on Geoscience and Remote Sensing*, vol. 52, no. 6, pp. 3553–3567, 2014. 815

816

[17] P. Salembier and S. Foucher, "Optimum graph cuts for pruning binary partition trees of polarimetric SAR images," *IEEE Transactions on Geoscience and Remote Sensing*, vol. 54, no. 9, pp. 5493–5502, 2016. 819

820

[18] B. Pang, S.-q. Xing, Y.-z. Li, and X.-s. Wang, "Speckle filtering algorithm for polarimetric SAR based on mean shift," in *2012 IEEE International Geoscience and Remote Sensing Symposium*, 2012, pp. 5892–5895. 823

824

[19] B. Pang, S. Xing, Y. Li, and X. Wang, "Novel polarimetric SAR speckle filtering algorithm based on mean shift," *Journal of Systems Engineering and Electronics*, vol. 24, no. 2, pp. 222–223, 2013. 825

826

[20] J.-S. Lee, T. L. Ainsworth, Y. Wang, and K.-S. Chen, "Polarimetric SAR speckle filtering and the extended Sigma filter," *IEEE Transactions on Geoscience and Remote Sensing*, vol. 53, no. 3, pp. 1150–1160, 2015. 827

828

[21] A. K. Jain, "Data clustering: 50 years beyond k-means," *Pattern Recognition Letters*, vol. 31, no. 8, pp. 651–666, 2010, award winning papers from the 19th International Conference on Pattern Recognition (ICPR). [Online]. Available: https://www.sciencedirect.com/science/article/pii/S0167865509002323 829

830

831

832

833

834

835

836

837

838

839

- 840 [22] S. Borra, R. Thanki, and N. Dey, *Satellite Image Analysis: Clustering and Classification*. Springer Nature, Singapore, 2019.
- 841
- 842 [23] J. S. Lee, M. R. Grunes, and R. Kwok, "Classification of multi-look polarimetric SAR imagery based on complex Wishart distribution," *International Journal of Remote Sensing*, vol. 15, no. 11, pp. 2299–2311, 1994. [Online]. Available: <https://doi.org/10.1080/01431169408954244>
- 843
- 844
- 845
- 846
- 847 [24] S. Cloude and E. Pottier, "An entropy based classification scheme for land applications of polarimetric sar," *IEEE Transactions on Geoscience and Remote Sensing*, vol. 35, no. 1, pp. 68–78, 1997.
- 848
- 849
- 850 [25] G. Vasile, J.-P. Ovarlez, F. Pascal, and C. Tison, "Coherency matrix estimation of heterogeneous clutter in high-resolution polarimetric SAR images," *IEEE Transactions on Geoscience and Remote Sensing*, vol. 48, no. 4, pp. 1809–1826, 2010.
- 851
- 852
- 853
- 854 [26] A. Alonso-Gonzalez, C. Lopez-Martinez, and P. Salembier, "Filtering and segmentation of polarimetric SAR data based on binary partition trees," *IEEE Transactions on Geoscience and Remote Sensing*, vol. 50, no. 2, pp. 593–605, 2012.
- 855
- 856
- 857
- 858 [27] S. Foucher and C. López-Martínez, "Analysis, evaluation, and comparison of polarimetric SAR speckle filtering techniques," *IEEE Transactions on Image Processing*, vol. 23, no. 4, pp. 1751–1764, 2014.
- 859
- 860
- 861
- 862 [28] S. Cloude, *Polarisation: Applications in Remote Sensing*. Oxford University Press, Oxford, 2009.
- 863
- 864 [29] C. C. Lee, "Elimination of redundant operations for a fast Sobel operator," *IEEE Transactions on Systems, Man, and Cybernetics*, vol. SMC-13, no. 2, pp. 242–245, 1983.
- 865
- 866
- 867 [30] P. Mather and M. Koch, *Computer Processing of Remotely-Sensed Images: An Introduction, Fourth Edition*. John Wiley and Sons Ltd, UK, 2011.
- 868
- 869
- 870 [31] L. Thirion-Lefevre and R. Guinvarc'h, "The double Brewster angle effect," *Comptes Rendus Physique*, vol. 19, no. 1, pp. 43–53, 2018. [Online]. Available: <https://www.sciencedirect.com/science/article/pii/S1631070518300173>
- 871
- 872
- 873
- 874 [32] J. Polcari, "Butterfly decomposition of arbitrary unitary matrices," Working Paper, 2014.
- 875
- 876 [33] J. Chen, H. Zhang, C. Wang, and J. Jia, "Roll-invariant target parameter extraction from POLSAR data," *IEEE Journal of Selected Topics in Applied Earth Observations and Remote Sensing*, vol. 12, no. 11, pp. 4502–4516, 2019.
- 877
- 878
- 879
- 880 [34] B. Souissi and M. Ouarzeddine, "Analysis of orientation angle shifts on the polarimetric data using Radarsat2 images," *IEEE Journal of Selected Topics in Applied Earth Observations and Remote Sensing*, vol. 9, no. 4, pp. 1331–1342, 2016.
- 881
- 882
- 883
- 884 [35] N. Gasnier, L. Denis, and F. Tupin, "On the use and denoising of the temporal geometric mean for SAR time series," *IEEE Geoscience and Remote Sensing Letters*, vol. 19, pp. 1–5, 2022.
- 885
- 886
- 887 [36] F. Yang, W. Gao, B. Xu, and J. Yang, "Multi-frequency polarimetric SAR classification based on Riemannian manifold and simultaneous sparse representation," *Remote Sensing*, vol. 7, no. 7, pp. 8469–8488, 2015. [Online]. Available: <https://www.mdpi.com/2072-4292/7/7/8469>
- 888
- 889
- 890
- 891
- 892 [37] H. Song, W. Yang, N. Zhong, and X. Xu, "Unsupervised classification of PolSAR imagery via kernel sparse subspace clustering," *IEEE Geoscience and Remote Sensing Letters*, vol. 13, no. 10, pp. 1487–1491, 2016.
- 893
- 894
- 895
- 896 [38] X. Yang, W. Yang, H. Song, and P. Huang, "Polarimetric SAR image classification using geodesic distances and composite kernels," *IEEE Journal of Selected Topics in Applied Earth Observations and Remote Sensing*, vol. 11, no. 5, pp. 1606–1614, 2018.
- 897
- 898
- 899
- 900
- 901 [39] J. Ren and X.-J. Wu, "Probability distribution-based dimensionality reduction on Riemannian manifold of SPD matrices," *IEEE Access*, vol. 8, pp. 153 881–153 890, 2020.
- 902
- 903